TU Delft

Delft University of Technology

Document Version
Final published version

Licence
Dutch Copyright Act (Article 25fa)

Citation (APA)
Yang, Z., Sun, B., Wang, X., Zuo, Y., Tang, H., Zheng, C., Tang, Z., Zhang, G., & Fan, J. (2026). Temperature-governed lattice disorder, residual stress, and recovery in CVD 4H-SiC under Al implantation and annealing. *Journal of Alloys and Compounds*, *1054*, Article 186279. https://doi.org/10.1016/j.jallcom.2026.186279

Important note
To cite this publication, please use the final published version (if applicable).
Please check the document version above.

Copyright
In case the licence states “Dutch Copyright Act (Article 25fa)”, this publication was made available Green Open Access via the TU Delft Institutional Repository pursuant to Dutch Copyright Act (Article 25fa, the Taverne amendment). This provision does not affect copyright ownership.
Unless copyright is transferred by contract or statute, it remains with the copyright holder.

Sharing and reuse
Other than for strictly personal use, it is not permitted to download, forward or distribute the text or part of it, without the consent of the author(s) and/or copyright holder(s), unless the work is under an open content license such as Creative Commons.

Takedown policy
Please contact us and provide details if you believe this document breaches copyrights.
We will remove access to the work immediately and investigate your claim.

This work is downloaded from Delft University of Technology.

Journal of Alloys and Compounds 1054 (2026) 186279

Contents lists available at ScienceDirect

Journal of Alloys and Compounds

journal homepage: www.elsevier.com/locate/jalcom

Temperature-governed lattice disorder, residual stress, and recovery in CVD 4H-SiC under Al implantation and annealing

Zhoudong Yang [a], Botao Sun [b], Xinyue Wang [a], Yuanhui Zuo [b,*], Hongyu Tang [a], Changran Zheng [a], Zhuorui Tang [c], Guoqi Zhang [d], Jiajie Fan [a,b,d,**]

[a] Shanghai Engineering Technology Research Center for SiC Power Device, College of Intelligent Robotics and Advanced Manufacturing, Fudan University, Shanghai 200433, China
[b] Research Institute of Fudan University in Ningbo, Ningbo 315336, China
[c] School of Electronic and Information Engineering, Foshan University, Foshan 528000, China
[d] EEMCS Faculty, Delft University of Technology, Delft 2628, the Netherlands

ARTICLE INFO

Keywords:
4H-SiC
Ion implantation
Temperature effects
Thermo-mechanical stress
Defect recovery
Molecular dynamics simulation
Micro-Raman spectroscopy

ABSTRACT

Ion implantation and subsequent annealing reshape the defect landscape and stress state of compound semiconductors, yet the temperature-dependent mechanisms in SiC remain incompletely understood. Here, we utilize molecular dynamics (MD) simulations and confocal micro-Raman measurements to resolve how implantation temperature and post-annealing regulate lattice disorder, amorphization kinetics, and residual-stress evolution in chemical vapor deposited (CVD) 4H-SiC. MD reveals surface-nucleated amorphization that propagates inward, whereas elevated implantation temperatures activate defect recombination pathways that suppress amorphous-layer formation. Raman signatures of optical-phonon shifts, linewidth broadening, and amorphization bands track the coupled evolution of lattice disorder and stress. Experimentally, increasing implantation temperature smooths the surface (S_a 0.133 → 0.101 nm) and reduces the amorphous-layer thickness (from ~700 nm at 25°C to undetectable at 500°C), while driving more compressive residual stress (−57 → −132 MPa). Post-annealing largely restores phonon lifetimes and eliminates amorphization signatures, consistent with the recovery trends predicted by MD. These results delineate a thermal-treatment window that controls amorphization and residual stress in 4H-SiC, providing a transferable Raman-based methodology for nondestructive assessment of implantation-induced damage in compound semiconductors.

1. Introduction

Efficient and precise element doping is the cornerstone of tailoring the electrical and optical properties of modern electronic and photonic devices [1–3]. While thermal diffusion has long enabled dopant incorporation in silicon-based devices [4–6], the intrinsic limitations of silicon become clear under the demands of broadband transparency, strong second-order nonlinearity, quantum color center integration, and reliable operation under extreme conditions (e.g., high frequency, high power, or high temperature)[7,8]. To meet these challenges, silicon carbide (SiC), particularly 4H-SiC, has emerged as a preferred material for next-generation power electronics and integrated/quantum photonic applications, including wide bandgap, high electron mobility, excellent thermal conductivity, robust electrical breakdown field, high refractive index, and strong optical nonlinearity [9–13]. However, the intrinsically low diffusion coefficients of dopant species in 4H-SiC preclude precise doping control via conventional diffusion, positioning ion implantation as the preferred technique for advanced device fabrication [14,15].

Ion implantation delivers atomic-scale dopant profiles through high-energy ion bombardment [16,17], yet simultaneously disrupts the crystal lattice, producing vacancies, interstitial clusters, and amorphous regions [18,19]. These can generate residual stress fields and degrade both electrical and optical performance [20]. High-temperature annealing is typically employed to repair implantation-induced damage and activate dopants [21]. Nevertheless, the extreme thermal stability of 4H-SiC demands annealing temperatures exceeding 1500°C

* Corresponding author.
** Corresponding author at: Shanghai Engineering Technology Research Center for SiC Power Device, College of Intelligent Robotics and Advanced Manufacturing, Fudan University, Shanghai 200433, China.
E-mail addresses: zuo_yuanhui@fudan.edu.cn (Y. Zuo), jiajie_fan@fudan.edu.cn (J. Fan).

https://doi.org/10.1016/j.jallcom.2026.186279
Received 30 October 2025; Received in revised form 30 December 2025; Accepted 17 January 2026
Available online 18 January 2026
0925-8388/© 2026 Elsevier B.V. All rights are reserved, including those for text and data mining, AI training, and similar technologies.

[22,23]. Such conditions often lead to surface roughening, unwanted 4 H → 3 C phase transitions [24], and incomplete defect recovery (even with protective coatings [25]), thereby limiting device yield and reliability. While these challenges have spurred interest in low-temperature annealing techniques [26], another promising strategy lies in optimizing the ion implantation conditions, particularly the implantation temperature. Adjusting the implantation temperature can directly influence defect generation, stress evolution, and the efficiency of subsequent thermal recovery. Defect damage and residual stress are crucial to the actual electrical and optical performance in electronic and photonic devices [27,28]. Despite previous studies that have extensively explored the impact of parameters such as dose, energy, and implantation angle on crystal damage [29–34], the critical role of implantation temperature on lattice damage and residual stress evolution remains unclear.

In this work, we introduce a nondestructive, multiscale strategy that utilizes molecular dynamics (MD) simulations and confocal micro-Raman spectroscopy to address the limitations of conventional approaches. Specifically, the MD simulations and micro-Raman measurements are performed independently, and their results are subsequently correlated at the interpretation level. MD reveals that elevating the implantation temperature activates dynamic self-repair pathways that suppress amorphization while concurrently increasing compressive residual stress. Complementary micro-Raman mapping provides spatially resolved optical-phonon frequency shifts and linewidth broadening that directly track the coupled progression of lattice disorder and stress. The combined evidence delineates thermally governed pathways for damage generation and recovery, establishing a transferable research framework for non-destructive assessment of implantation-induced structural damage and stress in wide-bandgap compound semiconductors.

2. Experimental section

2.1. Sample preparation

The samples studied in this experiment were 6-inch commercial 4H-SiC homoepitaxial wafers prepared by chemical vapor deposition (CVD), with an epitaxial layer thickness of 10 μm (China Electronics Compound Semiconductor Co., Ltd., China). Al ion implantation was performed at 25°C, 350°C, and 500°C using an HY-IMP-E400A ion implanter, with a single-energy, single-step implantation at 600 keV and an implantation dose of 10^{14} ions cm^{-2}. These three implantation temperatures were selected to span a practical processing window [35]: 25°C as a room-temperature baseline, 350°C as an intermediate condition to probe the transition regime where dynamic defect recombination starts to compete with damage accumulation, and 500°C as a high-temperature condition to enhance dynamic self-healing during implantation. This design enables a clear temperature-dependent comparison under identical implantation energy and dose. Single implantation was chosen to maintain the implantation condition identical across all temperatures, thereby facilitating studies on temperature-related mechanisms. Subsequently, post-implant high-temperature annealing was conducted in an automatic rapid thermal processing system (HY-RTP 200) under a pure Ar atmosphere at 1750°C for 30 min, as shown in Fig. 1. The post-implant annealing condition (1750°C for 30 min in Ar) was chosen as a representative high-temperature recovery/activation treatment for Al-implanted 4H-SiC, providing substantial defect recovery while avoiding unnecessarily prolonged thermal exposure [35–37]. During annealing, a carbon-based protective cap (C-cap/graphite-type layer) was applied to mitigate Si sublimation and prevent surface degradation/roughening, which is commonly used in SiC high-temperature processing [30,36].

2.2. Characterization and measurements

The surface roughness of the wafers, both before and after ion implantation, was measured using atomic force microscopy (AFM, Bruker/Dimension Icon, Germany). The AFM was equipped with a SCANASYST-FLUID+ probe (tip radius approximately 2 nm; length 70 μm; width 10 μm) to acquire AFM morphology images in tapping mode. The scanning area is 5 μm × 5 μm, and the image sampling rate is 512 × 512 pixels. Raman testing was performed using a HORIBA micro-Raman spectrometer (Japan), and the single-crystal silicon peak at 520.7 cm^{-1} was used for spectral calibration before testing. The experiment utilized a 100 × lens for backscattered light signals, with a grating density of 1800 gr/mm, and the laser used a wavelength of 532 nm. The laser power for the test was set to 5 % of the total intensity (50 mW).

2.3. Molecular dynamics simulation

MD simulations were performed using the Large-Scale Atomic/Molecular Massively Parallel Simulator (LAMMPS), while visualization and data analysis were conducted using the Open Visualization Tool (OVITO). A 4H-SiC slab was constructed along the [0001] crystal direction for ion implantation simulations. The slab dimensions are 10.56 nm × 10.19 nm × 17.89 nm, with periodic boundary conditions applied in the X and Y directions. As shown in Fig. 2, the slab is divided into three regions: the boundary layer, the thermostatic layer, and the Newtonian layer. The boundary layer, comprising the bottom four atomic layers, is fixed to ensure structural stability. The thermostatic layer and the Newtonian layer are governed by different ensembles. Specifically, the thermostatic layer is treated with the NVT ensemble to dissipate the heat generated by Al ion implantation and maintain a constant temperature by regulating atomic velocities. During ion bombardment, temperature control is only applied to this region. In contrast, the Newtonian layer uses the NVE ensemble, allowing it to capture the cascade collision events induced by the implanted ions and thereby elucidate the resulting lattice damage distribution. Ion implantation was simulated on the 4H-SiC surface at various temperatures,

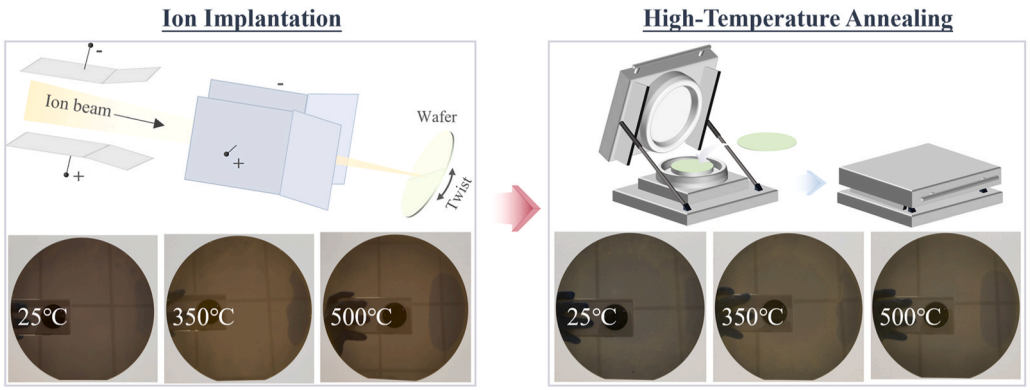


Fig. 1. Schematic of Al ion implantation into a 4H-SiC homoepitaxial wafer, the post-implantation annealing, and the corresponding prepared samples.

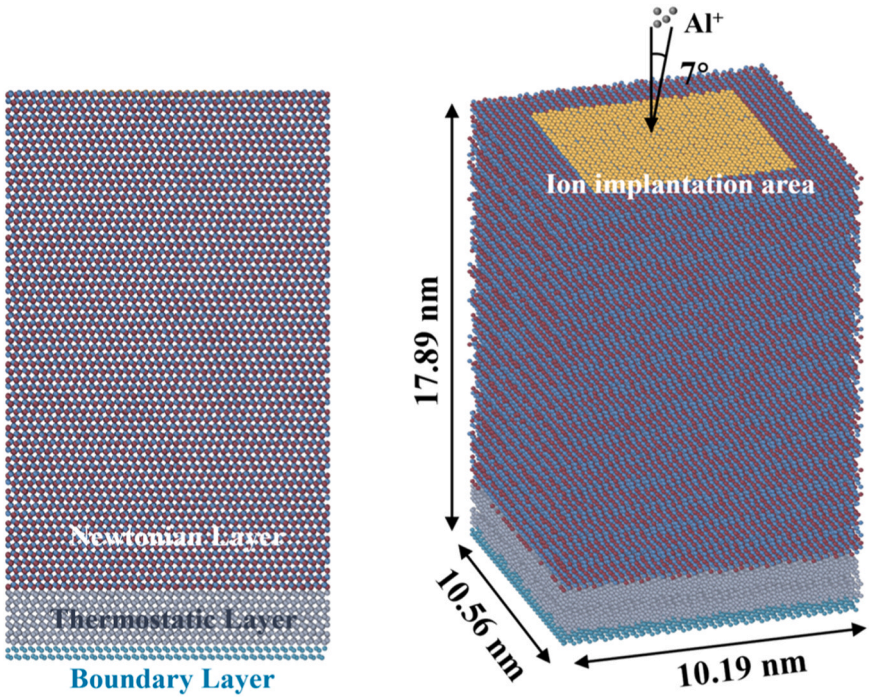


Fig. 2. Atomistic molecular dynamics model for Al ion implantation in 4H-SiC.

with an implantation energy set to 2 keV and a 20 ps interval between each ion. An annealing process was then performed on the entire model following ion implantation. During these simulations, both the GW-ZBL potential and the embedded-atom method (EAM) potential were employed: GW-ZBL described interactions within 4H-SiC, while EAM accounted for the interactions of implanted Al atoms. The cross-interactions between Al–Si and Al–C atoms were represented by a Morse potential derived from ab initio calculations. Finally, compression deformation simulations of the model were conducted before and after annealing to obtain stress–strain curves under each condition. It should be noted that the implantation energy used in MD (2 keV) is different from the experimental energy (600 keV) due to the computational constraints of explicitly resolving collision cascades at hundreds of keV within a ~10 nm-scale cell [38,39]. Accordingly, the MD simulations in this work are designed to capture the temperature-dependent microscopic mechanisms (collision-cascade damage accumulation, dynamic defect recombination, amorphization tendency, and stress evolution) rather than to reproduce the absolute implanted depth profile at 600 keV. The post-implantation "annealing" step in MD is a short-timescale thermal relaxation within accessible simulation time, introduced to assess the relative recovery tendency after implantation, whereas the experimental annealing involves a much larger thermal budget (high-temperature furnace anneal for minutes). In addition, the simulated 4H-SiC slab is constructed along the [0001] direction without the 4° wafer offcut, consistent with current simulation modeling in existing literature [38–41].

2.4. Monte Carlo simulation

The state of Al ion implantation in 4H-SiC crystal was simulated using SRIM-2013 software (with detailed calculation of the complete damage cascade). The threshold displacement energies of carbon and silicon were set to 20 eV and 35 eV [42,43], respectively, and the lattice binding energy was zero [44]. The density of 4H-SiC was 3.21 g cm^{-3}. The Al ion implantation energy was 600 keV, which was consistent with the actual sample implantation parameters. Therefore, SRIM is primarily used here to determine implantation depth/damage distribution and supplement the mechanistic trends revealed by MD.

3. Results and discussion

3.1. MD simulation of Al ion implanted 4H-SiC

MD simulations are a powerful tool for exploring atomic/nanoscale mechanisms, complementing experimental methods [41,45]. In this study, an MD model was constructed to predict the effects of implantation temperature on Al ion implantation into 4H-SiC and to simulate the subsequent annealing process. Figs. 3a and S1 show the surface topological damage of 4H-SiC at various implantation temperatures after Al ion implantation and high-temperature annealing, respectively. The simulations reveal that the Al ion beams induce a sputtering effect on the 4H-SiC surface, forming sharp pits accompanied by atomic accumulation and swelling around these pits due to the cascade motion of surface atoms. This phenomenon is most pronounced at 25°C and decreases with increasing implantation temperature. The evolution of surface damage with implantation temperature was quantified using arithmetic mean roughness (S_a) and root mean square roughness (S_q), highlighting the positive role of higher implantation temperature in surface repair, as shown in Fig. 3b. Additionally, high-temperature annealing significantly mitigated surface topological damage across all implantation temperatures.

Further, the effect of Al ions on the internal crystal damage of 4H-SiC at different implantation temperatures was analyzed using the identification of diamond structures (IDS) method [39]. Fig. S2 depicts the pristine 4H-SiC lattice before ion implantation, serving as a reference. In the IDS classification, the "other" category represents the severely damaged (amorphized) lattice regions; the cubic diamond and hexagonal diamond areas denote undamaged areas, while the first and second neighbor structures indicate slightly displaced and markedly damaged states, respectively [38]. The simulation results demonstrate that high-energy Al ions induce crystal damage along their trajectories, accumulating damage during implantation (Fig. 4). Severe amorphization is primarily localized near the surface, underscoring the strong correlation between initial ion collisions and surface damage. As the implantation temperature increases, the severity and extent of internal damage substantially decrease, indicating that higher temperatures enhance defect repair mechanisms. Furthermore, although implantation

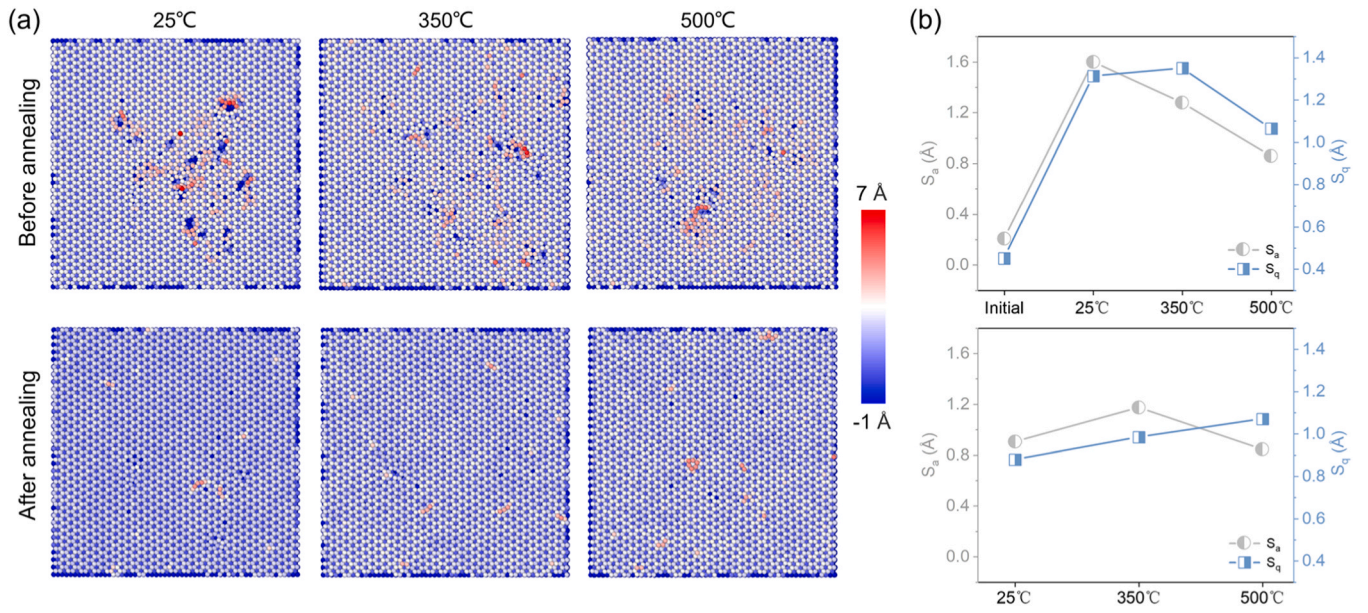


Fig. 3. Molecular dynamics simulations of 4H-SiC surface damage at different Al implantation temperatures and after annealing: (a) spatial distribution of surface damage; (b) surface roughness statistics.

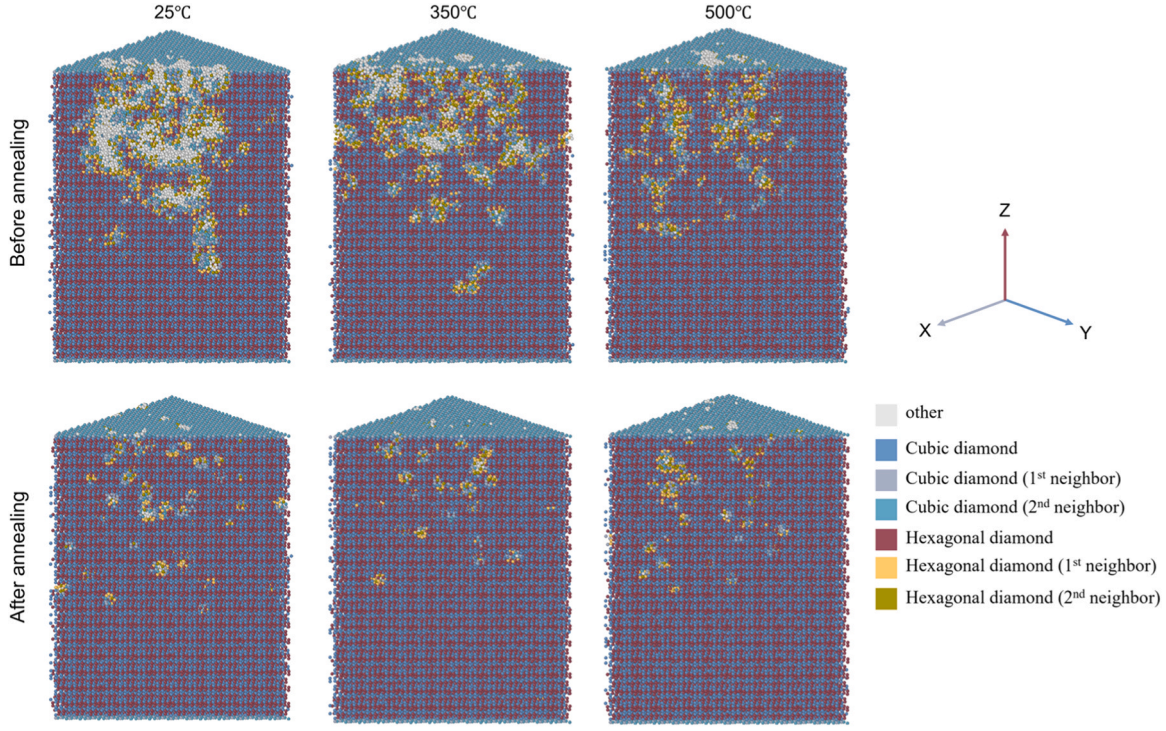


Fig. 4. Cross-sectional views from molecular dynamics simulations showing the internal damage distribution in 4H-SiC after Al ion implantation and subsequent annealing at different temperatures. The diagonal cross-section has a height of 17.89 nm and a diagonal length of ~14.67 nm.

damage is concentrated in the ion implantation area, the damage extends to the non-implantation area due to the cascade collisions from high-energy ion implantation impacts (Fig. S3). High-temperature annealing effectively repairs this damage, eliminating severe amorphization.

We further quantified vacancies and interstitial atoms using the Wigner-Seitz (WS) defect method to examine the microscopic change trends during Al ion implantation at different implantation temperatures [40,46]. At 25°C, the vacancy and interstitial defect concentration were approximately 2.2×10^{21} cm^{-3}. As the implantation temperature increased, the defect concentration decreased, dropping to 4.05×10^{20} cm^{-3} at 500°C (Fig. 5a). This reduction confirms that higher temperatures facilitate defect repair. High-temperature annealing further reduced defect concentrations (Fig. 5b), reinforcing the role of elevated temperatures in mitigating implantation-induced damage.

To investigate the impact of implantation temperatures on the crystal's atomic structure, the radial distribution function (RDF) was calculated for the ion implantation, bottom, and overall regions (see Note S1 in the Supporting Information for details). The RDF peaks at 1.875 Å and 3.075 Å correspond to the nearest neighbor distances

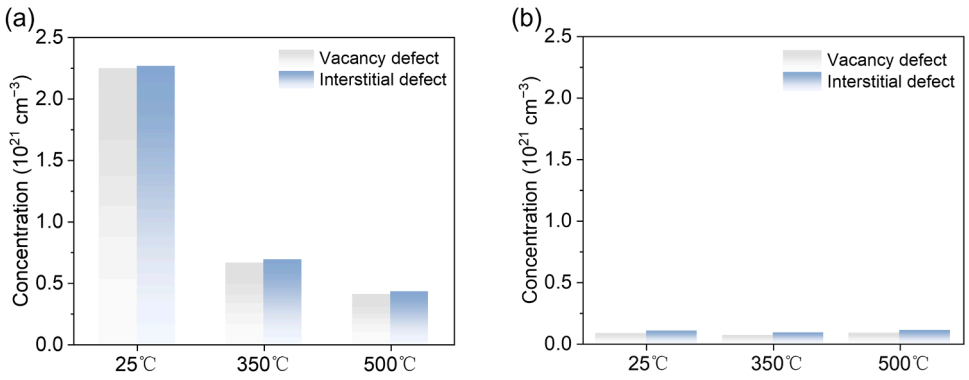


Fig. 5. Statistics of vacancy and interstitial concentrations inside 4H-SiC at different ion implantation temperatures: (a) before annealing; (b) after annealing.

between C-Si, C-C, and Si-Si atoms, respectively, as shown in Figs. 6a and 6b. These are consistent with the bond length values obtained from the 4H-SiC crystal structure (C-Si: 1.895 Å; C-C: 3.094 Å, and Si-Si: 3.098 Å). Post-implantation, the most substantial decrease in RDF peak intensity in the ion implantation area was at 25°C, indicating the highest degree of crystal structure damage under these conditions. Ion implantation disrupts atomic bonding energy, reducing RDF peak intensities, broadening peak widths, and causing peak asymmetry, particularly within the 3–5 Å atomic distance range. These changes reflect covalent bond disruption and disorder resulting from cascade collisions. Higher implantation temperatures mitigate these effects, enhancing bonding strength and promoting partial self-repair. Notably, no graphitization characteristic peak (1.575 Å) was observed at any implantation temperature [47], indicating that the crystal structure remained largely intact. The RDF analyses of the bottom and overall regions further confirm limited crystal damage and the preservation of structural order. After high-temperature annealing, the RDFs of all samples nearly matched their initial states, indicating effective internal damage repair.

To probe the local structural environment of implanted Al, we

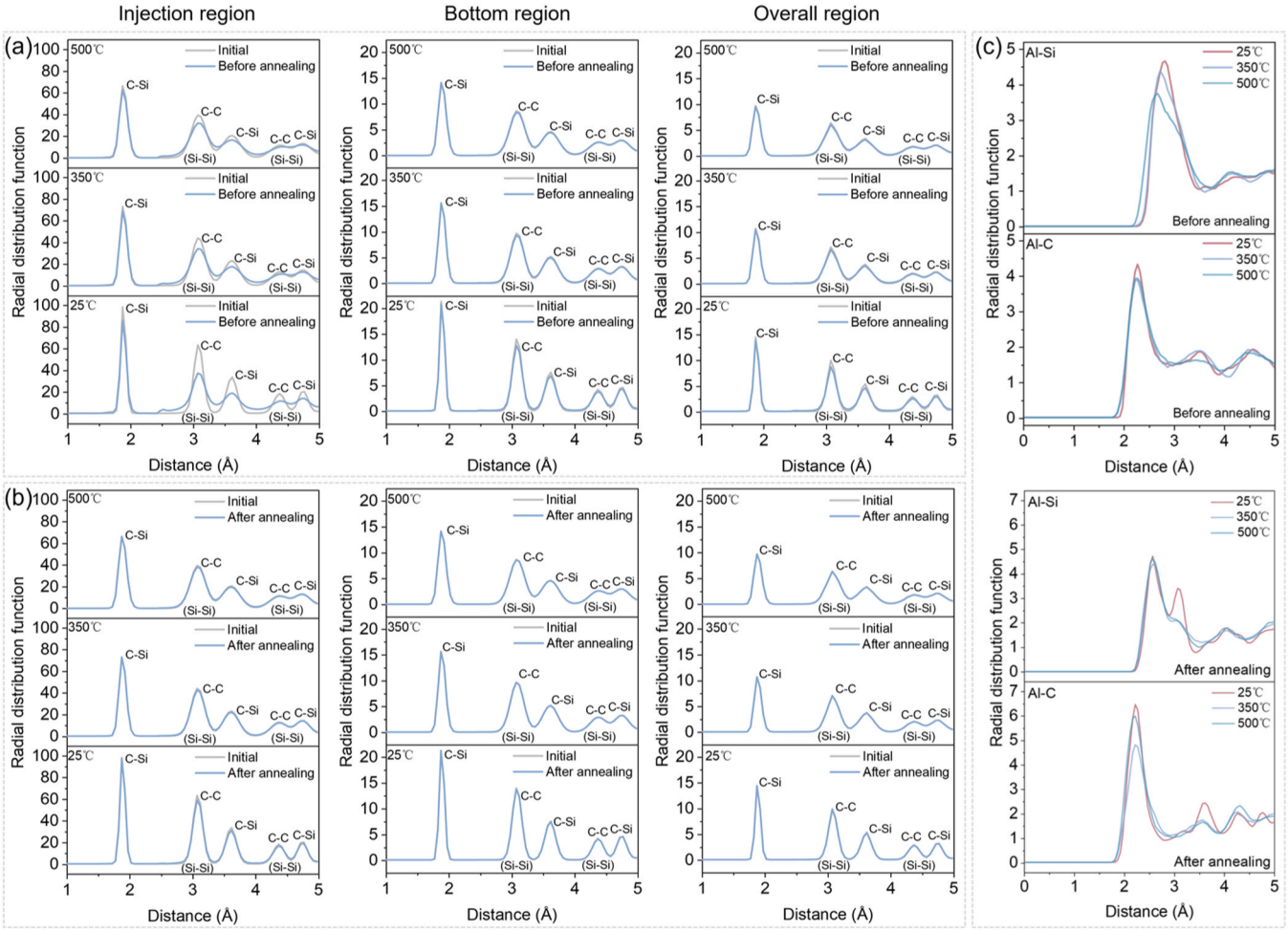


Fig. 6. Calculation of radial distribution function of 4H-SiC at different Al ion implantation temperatures and after annealing. (a) Radial distribution function results at different implantation temperatures. (b) Radial distribution function results after annealing. (c) Al-Si and Al-C atomic distances at different implantation temperatures and after annealing.

calculated the Al–Si and Al–C RDFs (Fig. 6c). With increasing implantation temperature, the characteristic RDF peaks for both Al–Si and Al–C become lower and slightly broader, consistent with stronger thermal vibrations (thermal broadening) and temperature-assisted atomic rearrangement during implantation. For Al–Si, the dominant first-shell peak progressively shifts to shorter distances from ~2.825 Å (25°C) to ~2.725 Å (350°C) and ~2.675 Å (500°C), indicating a more compact/ordered first-shell Al–Si configuration at higher implantation temperatures. Notably, no clear Al–Si feature occurs near ~3.0 Å before annealing; after annealing, a distinct ~3.0 Å correlation appears only for the 25°C-implanted case, which we attribute to the development/enhancement of second-shell (medium-range) Al–Si correlation during post-annealing structural recovery and Al redistribution in the more heavily damaged low-temperature sample [48,49]. After annealing, the dominant Al–Si first-shell correlation relaxes and stabilizes at ~2.575 Å. For Al–C, the main-peak position remains nearly unchanged across implantation temperatures, whereas its peak height decreases with increasing temperature both before and after annealing, suggesting that the characteristic near-neighbor Al–C distance is preserved while the local coordination environment becomes more distributed at higher temperatures. In addition, the medium-range feature near ~3.6 Å is selectively strengthened after annealing at 25°C, consistent with more substantial structural reconstruction enabled by the higher initial defect density compared with the 350/500°C cases [50].

Defects introduced by ion implantation in 4H-SiC can substantially degrade the mechanical performance of the material. To investigate the effect of different implantation temperatures on the mechanical properties of 4H-SiC, we conducted compression simulations on 4H-SiC samples implanted at various temperatures and performed additional compression simulations on the annealed samples to evaluate the extent of property recovery following annealing. These simulations were carried out within a 20 % compressive strain range, and the results are shown in Fig. 7. All stress-strain curves exhibit a distinct "turning point", where the slope markedly decreases, signifying the transition from elastic to plastic deformation. To facilitate interpretation of the elastic–plastic transition and the subsequent damage evolution, the insets in Fig. 7 present representative atomic-structure snapshots of the implanted region taken at two characteristic stages: the onset of plasticity (near the turning point) and the end of deformation (20 % strain). Moreover, a comparison of samples indicates that the large number of defects introduced by ion implantation narrows the elastic deformation region and extends the plastic deformation region of 4H-SiC. This is primarily due to the restricted dislocation motion and planar slip characteristic of covalently bonded materials such as SiC, which generally exhibit high hardness and brittleness at the macroscopic level. The presence of abundant defects, however, can markedly facilitate dislocation motion and planar slip, thereby enhancing the plasticity of the material. Compared to samples implanted at lower temperatures, those subjected to high-temperature ion implantation show a higher elastic-plastic transition stress (> 60 GPa) and exhibit strength characteristics

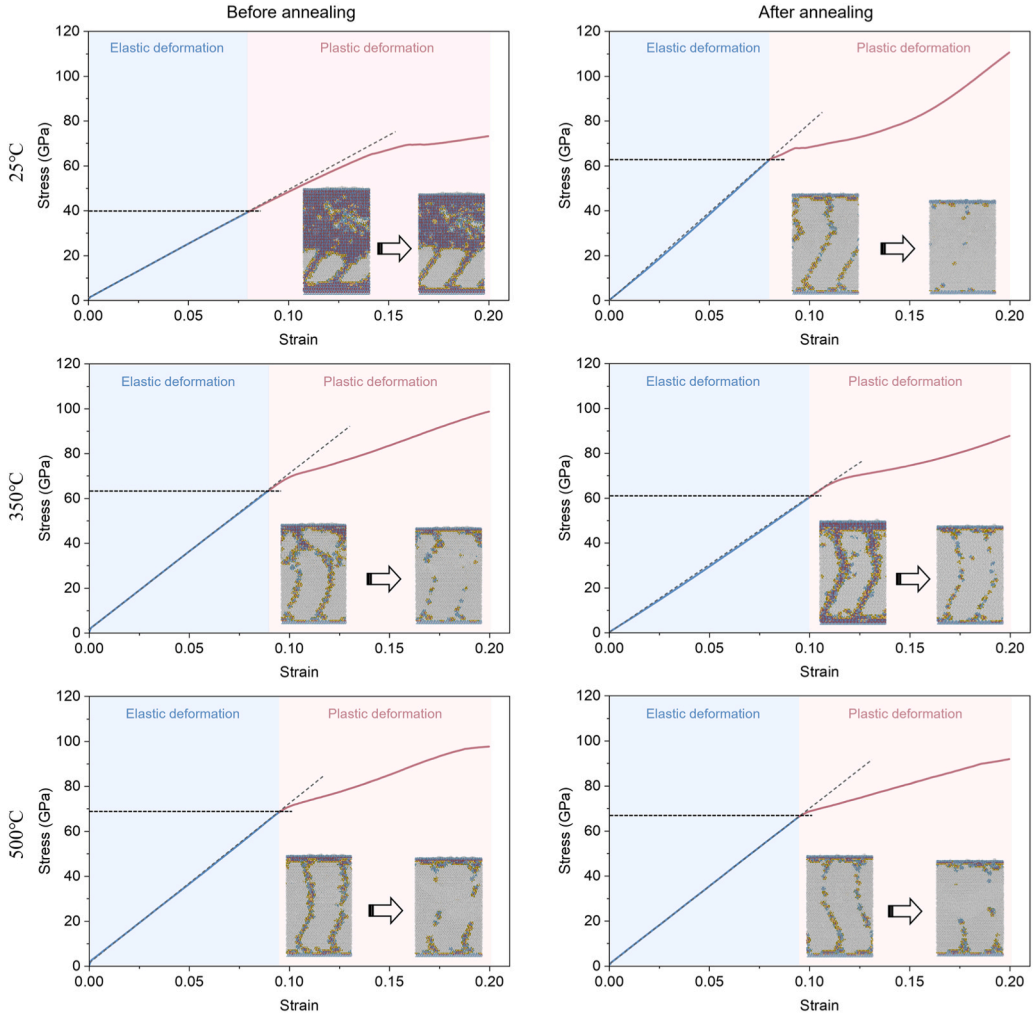


Fig. 7. Mechanical properties of 4H-SiC crystal after different implantation temperatures and annealing. The inset shows representative MD simulation snapshots at the onset and termination of plastic deformation.

similar to the annealed samples. This observation suggests that high-temperature ion implantation effectively reduces defect accumulation and contributes to maintaining the intrinsic mechanical properties of 4H-SiC.

Ion implantation also induces residual stress in the surface and subsurface regions due to interatomic collisions, phase changes, and thermal effects. Figs. 8a and S4 show the spatial evolution of the stress field in 4H-SiC at different implantation temperatures. The stress is heterogeneous and primarily concentrates within the near-surface implanted/damaged zone, whereas the deeper region (especially near the bottom of the slab) is comparatively less affected. Contrary to the trend of decreasing damage with higher temperatures, residual stress

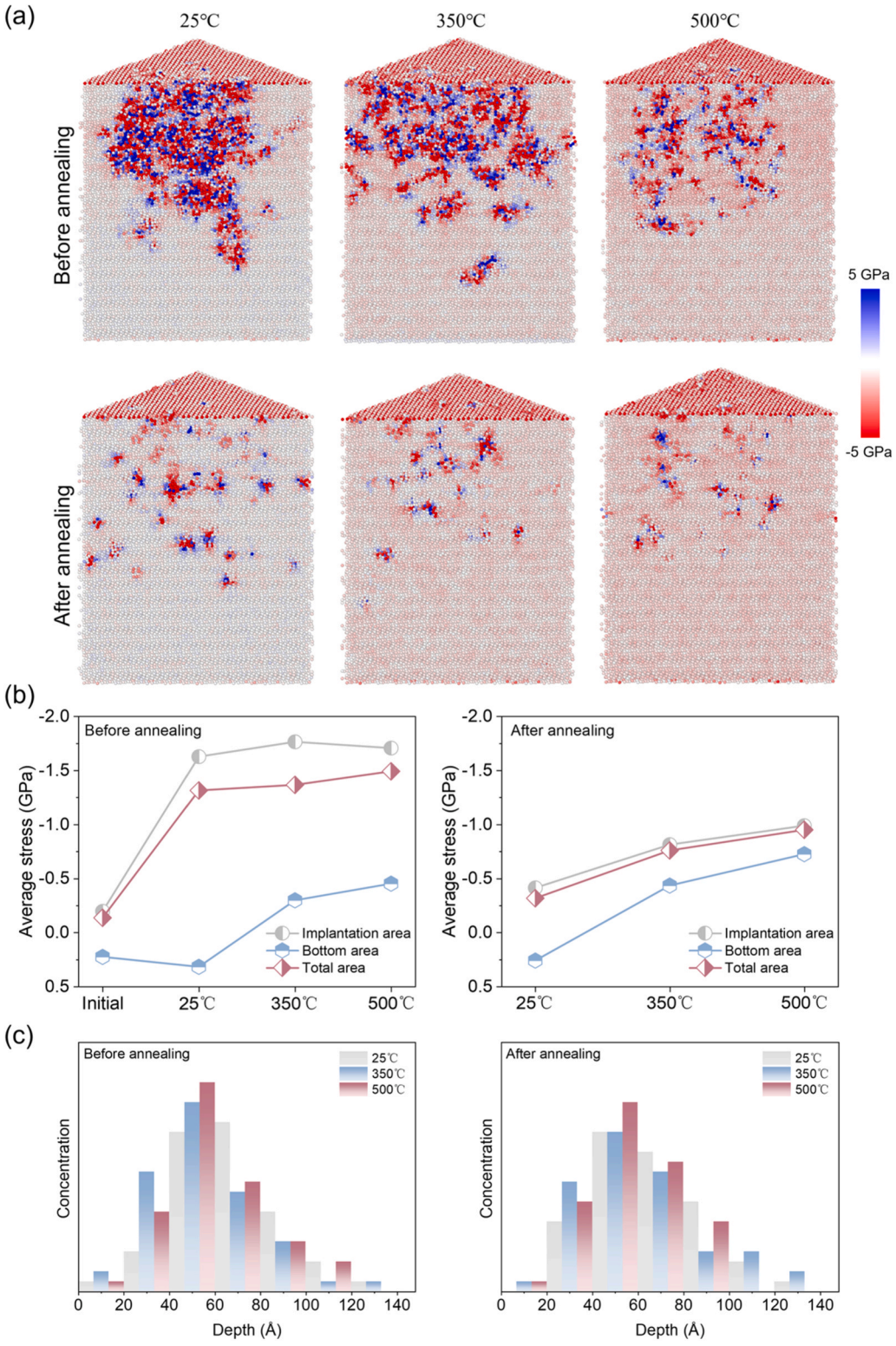


Fig. 8. Stress distribution and ion implantation depth in 4H-SiC crystal after different implantation temperatures and annealing. (a) Stress distribution (diagonal profile, height 17.89 nm, diagonal length approximately 14.67 nm). (b) Average stress changes with temperature. (c) Al ion implantation depth distribution statistics.

increases with temperature (Fig. 8b). This increase may result from enhanced thermal expansion and localized crystal repair, which exacerbate matrix inhomogeneity [51]. After high-temperature annealing, residual stress was substantially reduced, indicating effective stress relief. Ion implantation depth analysis showed that maximum residence depth after varying implantation temperatures and high-temperature annealing occurred between 40–60 Å (Fig. 8c), indicating the minimal impact of temperature on ion implantation depth and confirming the low thermal diffusion coefficient of Al in 4H-SiC. Notably, the predicted depth is derived from nanoscale MD simulations using a 2 keV implantation energy. Therefore, it is not comparable to the implantation depths measured in the subsequent experiments conducted at much higher energies and on macroscopic samples.

3.2. Experimental characterization and validation

To validate the accuracy of the MD simulation results, we performed Al ion implantation on 6-inch 4H-SiC epitaxial wafers under the same conditions used in our simulations. In the experiment, Al ions were implanted at a dose of 10^{14} ions cm^{-2}, with implantation temperatures of 25°C, 350°C, and 500°C, respectively. A pristine epitaxial wafer without implantation was used as a control sample for comparison (Fig. S5). Post-implantation characterization focused on crystal damage and residual stress, providing comparisons with the simulation predictions.

3.2.1. Lattice damage analysis

The roughness of the sample surface was measured by AFM, with the S_a value used to quantify the surface flatness changes, as shown in Fig. 9. The surface structure of the control sample exhibited a flat surface (S_a = 0.086 nm). When the implantation temperature was 25°C, ion implantation increased roughness to 0.133 nm, indicating marked surface damage. As the implantation temperature increased, the roughness gradually decreased to 0.119 nm at 350°C and 0.101 nm at 500°C, approaching the smoothness of the control wafer. These observations align with the MD simulation results, confirming that elevated implantation temperatures promote surface self-repair.

Micro-Raman spectroscopy further assessed crystal damage at different implantation temperatures. In particular, the E_2(TO) phonon mode full width at half maximum (FWHM) served as a sensitive indicator of lattice disorder. The multi-point Raman scan results of different samples indicate that ion implantation causes the FWHM value to increase, and the damage exhibits a high degree of inhomogeneity (Figs. 10a, c, and S6). The FWHM value of the blank sample is low and relatively concentrated. At 25°C, the FWHM value and distribution in the sample increase notably, indicating severe surface lattice disorder. At the higher implantation temperatures, the FWHM value gradually decreases, and the distributions become more uniform, highlighting the role of temperature in facilitating damage repair. Post-annealing Raman measurements validated these findings, showing marked FWHM reductions, especially in samples implanted at lower temperatures (Fig. 10b and d). Raman peak intensities also exhibited an inverse trend with FWHM, and post-annealing intensities further increased (Fig. 11). Under the same acquisition and processing conditions, the reduced peak intensity after implantation is mainly attributed to implantation-induced lattice disorder (amorphization/defect accumulation), which increases phonon scattering and decreases the Raman scattering efficiency of the crystalline mode. After high-temperature annealing, partial defect recovery and recrystallization reduce disorder, thereby increasing the intensity of the crystalline Raman peak.

Additionally, the structural damage inside the material will significantly affect the scattering process of phonons, thereby affecting the lifetime of phonons [52]. Therefore, we further calculated the change of E_2(TO) mode lifetime with implantation temperature using the energy-time uncertainty principle [53]:

$$\frac{2\pi\Gamma(T)}{h} = \frac{1}{\tau} \tag{1}$$

where $\Gamma(T)$ is the FWHM at the corresponding injection temperature, τ is the phonon lifetime, and $h = 3.3284 \times 10^{-11}$ cm^{-1} s is the Planck constant.

As shown in Fig. 12, phonon lifetimes decreased substantially after ion implantation. At 25°C and 350°C, the phonon lifetimes were similarly reduced; however, at 500°C, a notable recovery in lifetime was observed. Overall, the phonon-lifetime evolution exhibits an apparent threshold-like response within the investigated temperature window: the damage indicators remain comparably high at 25–350°C, but a marked recovery becomes evident at 500°C. This behavior suggests that dynamic defect recombination (self-healing) during implantation is substantially more effective in the 350–500°C interval under our experimental conditions. After high-temperature annealing, the 500°C-implanted samples exhibited the most distinct increase in phonon lifetime, highlighting the synergy between higher implantation temperatures and annealing in facilitating damage repair.

The full-spectrum Raman analysis revealed that compared with the initial Raman spectrum, ion implantation leads to new broad peaks, as

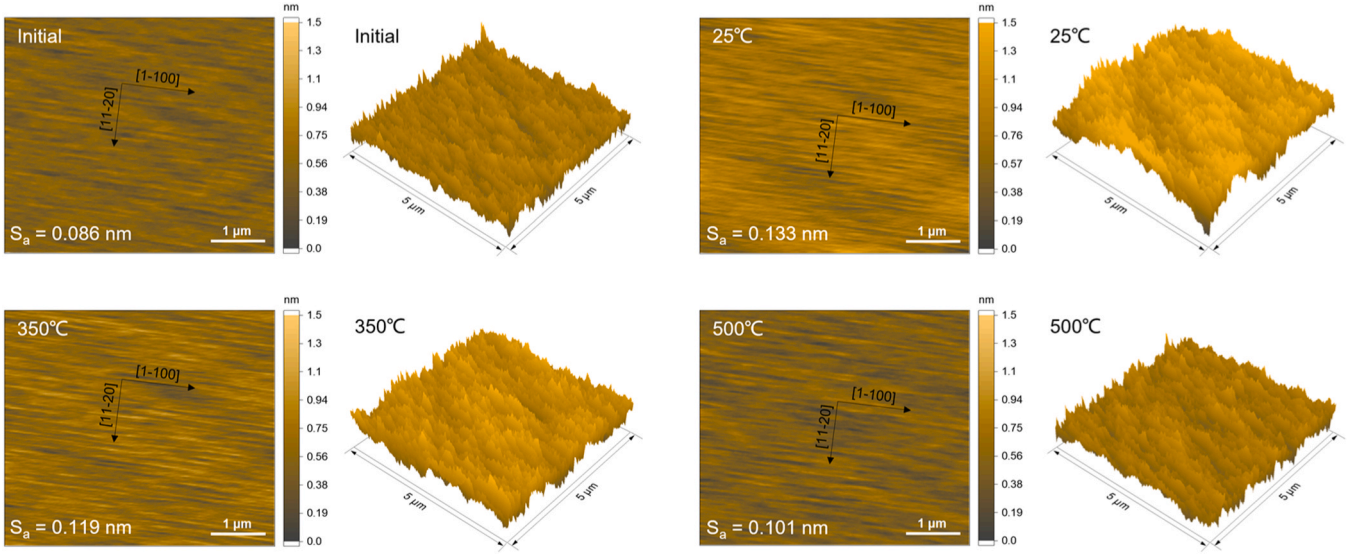


Fig. 9. Atomic force microscopy test of samples after ion implantation.

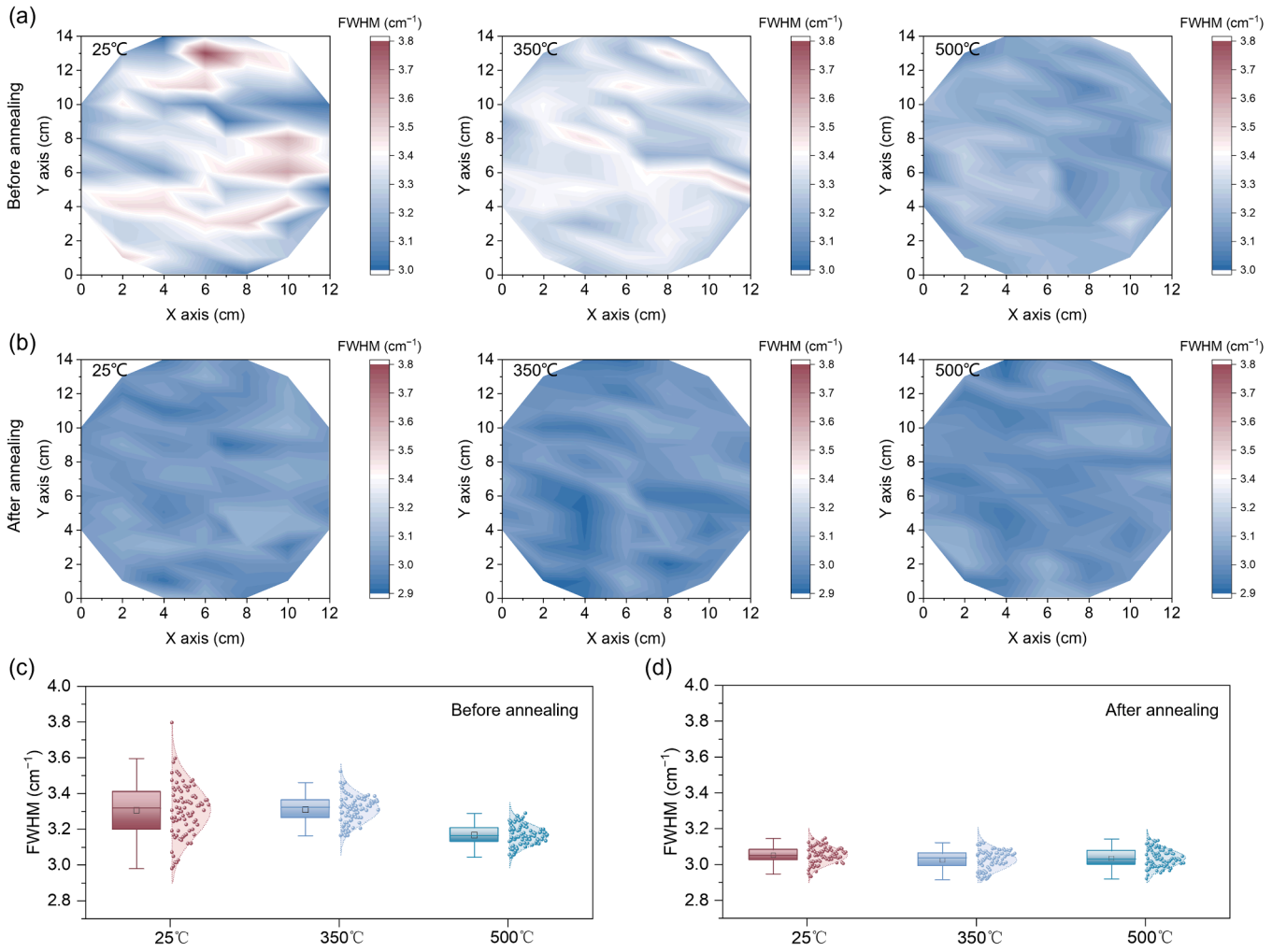


Fig. 10. Surface maps of the full width at half maximum (FWHM) of the E_2(TO) Raman peak: (a) after Al ion implantation and (b) after post-implantation annealing. (c, d) Corresponding FWHM statistics for the implanted and annealed states.

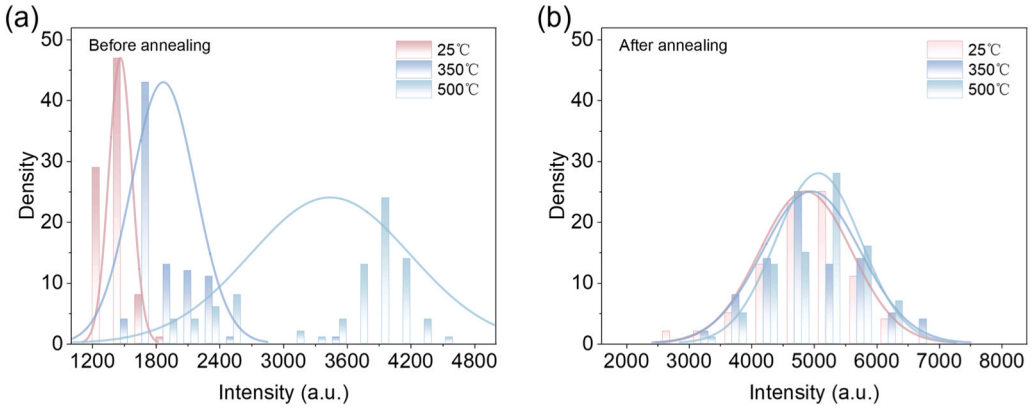


Fig. 11. E_2(TO) Raman peak intensity of 4H-SiC wafer after ion implantation and annealing: (a) After ion implantation; (b) After annealing. All Raman intensity maps were obtained using the same detection parameters.

shown in Fig. 13a. Specifically, there are "steamed bun-shaped" broad peaks in the three spectral regions of 150–350 cm^{-1}, 470–600 cm^{-1}, and 810–960 cm^{-1}. The reduction of the orderliness of the material's internal structure generally causes the appearance of such broad peaks [54]. Specifically, the broad peak at 470–600 cm^{-1} corresponds to amorphous Si-Si bonds, whereas the 150–350 cm^{-1} and 810–960 cm^{-1} arise from amorphous Si-C bonds [55,56]. These features diminished at higher implantation temperatures and vanished completely by 500°C, suggesting effective suppression or repair of amorphization. This trend matches the MD simulations' prediction of reduced crystal damage at elevated temperatures.

To further probe the depth profile of crystal damage by ion implantation under the influence of implantation temperature, we conducted a linear scan from the surface to a depth of 1 μm, as shown in

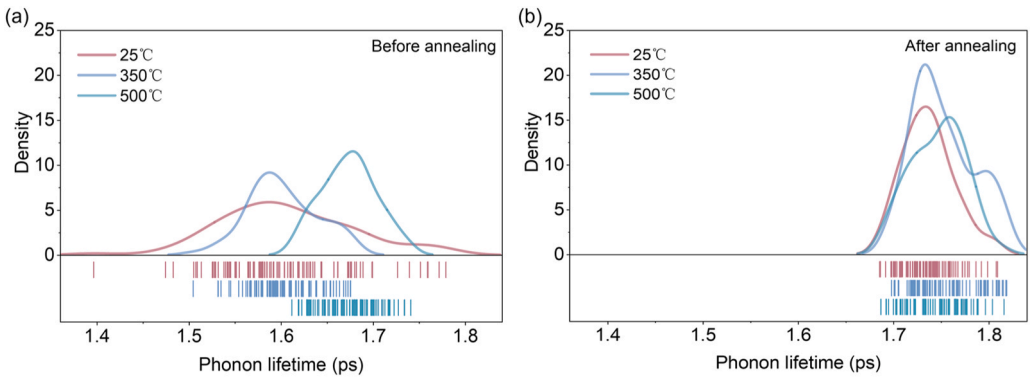


Fig. 12. E_2(TO) Phonon lifetime evaluation at different Al ion implantation temperatures of each sample (a) before annealing and (b) after annealing.

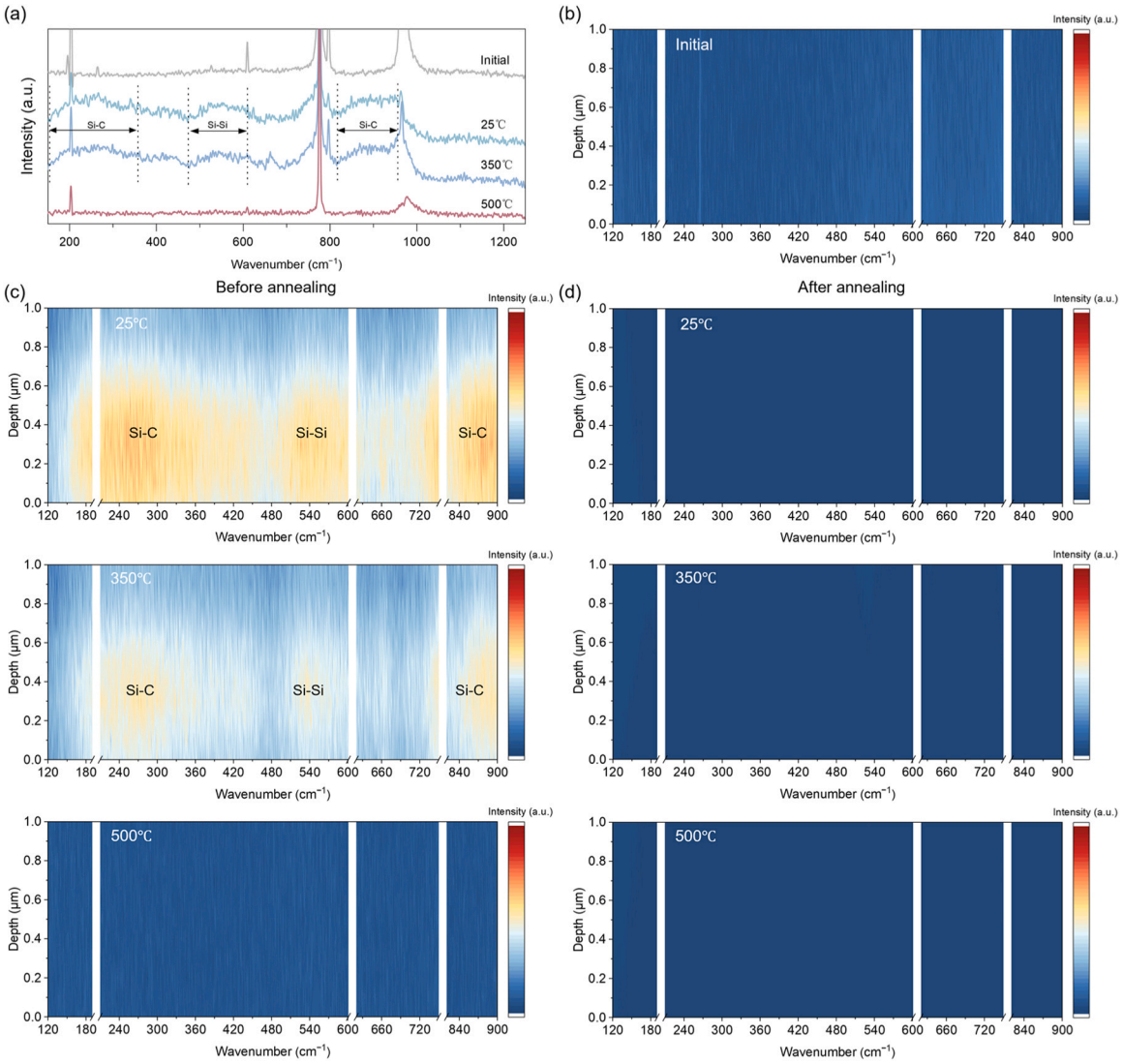


Fig. 13. Raman-based analysis of structural damage before and after ion implantation and annealing: (a) spectra of samples implanted at different temperatures; (b) Raman depth profile (0–1 μm) of the sample without ion implantation; (c) pre-annealing Raman depth profiles (0–1 μm); (d) post-annealing depth profiles (0–1 μm).

Figs. 13b and 13c. At 25°C, the amorphization damage depth extended to roughly 700 nm; the depth decreased to 600 nm at 350°C. At 500°C, no amorphization region was detected, indicating that higher implantation temperatures effectively repaired amorphous damage in 4H-SiC. These trends are consistent with both the pristine and the samples after annealing, as shown in Fig. 13d. Monte Carlo simulations estimated the amorphization threshold depth of approximately 670 nm (Fig. 14), consistent with experimental findings (the amorphization threshold of 4H-SiC is dpa = 0.28) [57,58]. To confirm that the lattice damage caused by ion implantation is limited to the top 1 μm, we further extended the focal depth scan to more than 1 μm, up to 14 μm. The results showed that no distinct damage occurred beyond a depth of 1 μm

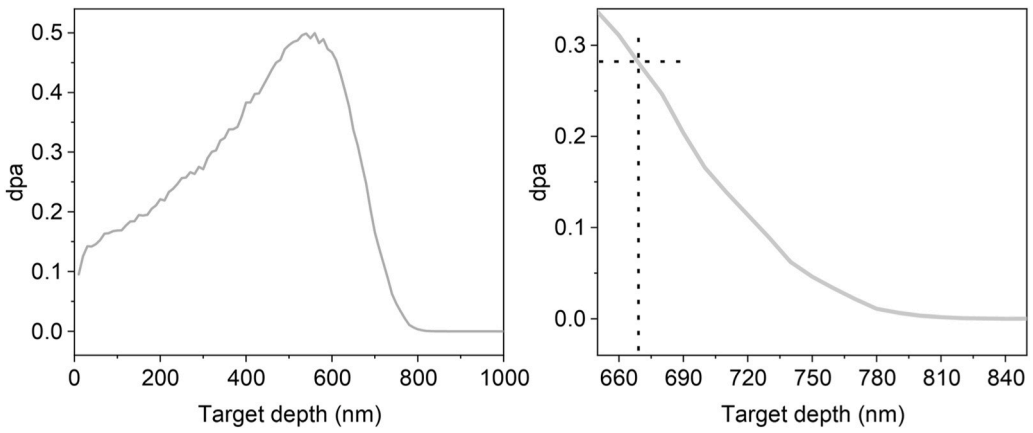


Fig. 14. Amorphization damage depth calculated based on Monte Carlo simulation (the right image is a magnified local version of the left image).

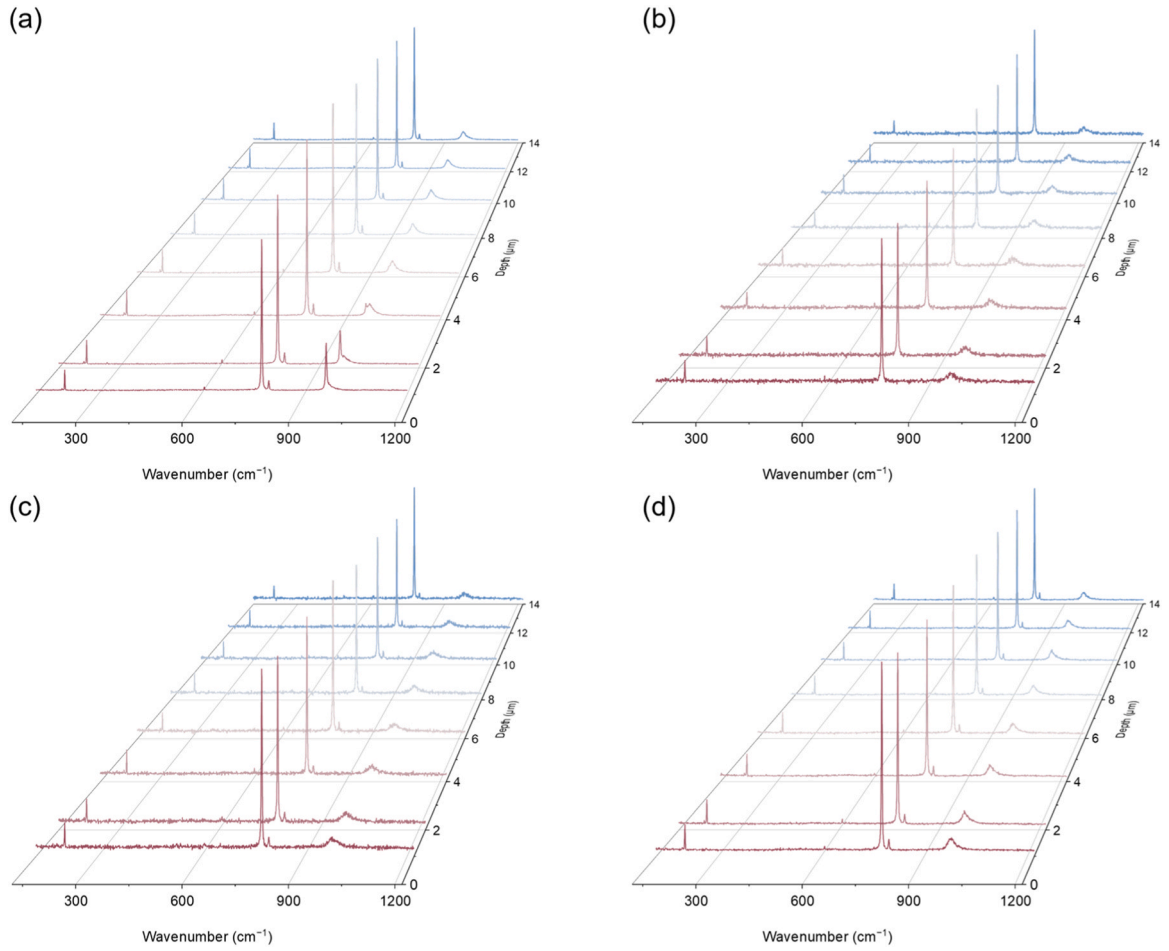


Fig. 15. Raman longitudinal depth test in the range of 1–14 μm at different ion implantation temperatures: (a) No ion implantation; (b) 25°C; (c) 350°C; (d) 500°C.

(Fig. 15). Finally, it should be noted that the simulations resolve microscale damage evolution within the near-surface implanted layer, whereas the Raman measurements provide a depth-resolved, nondestructive optical response that may include contributions from the underlying substrate. Therefore, these two approaches are complementary and together enable a more robust assessment of the evolution of ion implantation damage with temperature.

3.2.2. *Residual stress analysis*

Raman spectroscopy is also highly sensitive to the internal stress state of crystalline materials [59,60]. Here, we employed the peak shift of the E_2(TO) mode to evaluate the corresponding residual stress state of each sample, which is sensitive to in-plane stress. A single-point Raman measurement revealed that the control wafer exhibited its E_2(TO) peak at 777 cm^{-1}, indicating no residual stress [61,62] (Fig. 16a). After ion implantation, an obvious blue shift of the E_2(TO) peak was observed, corresponding to compressive stress in the wafer. The peak shift increased with implantation temperature, indicating higher residual stress at elevated temperatures. This trend underscores an important process trade-off: although higher implantation temperatures can

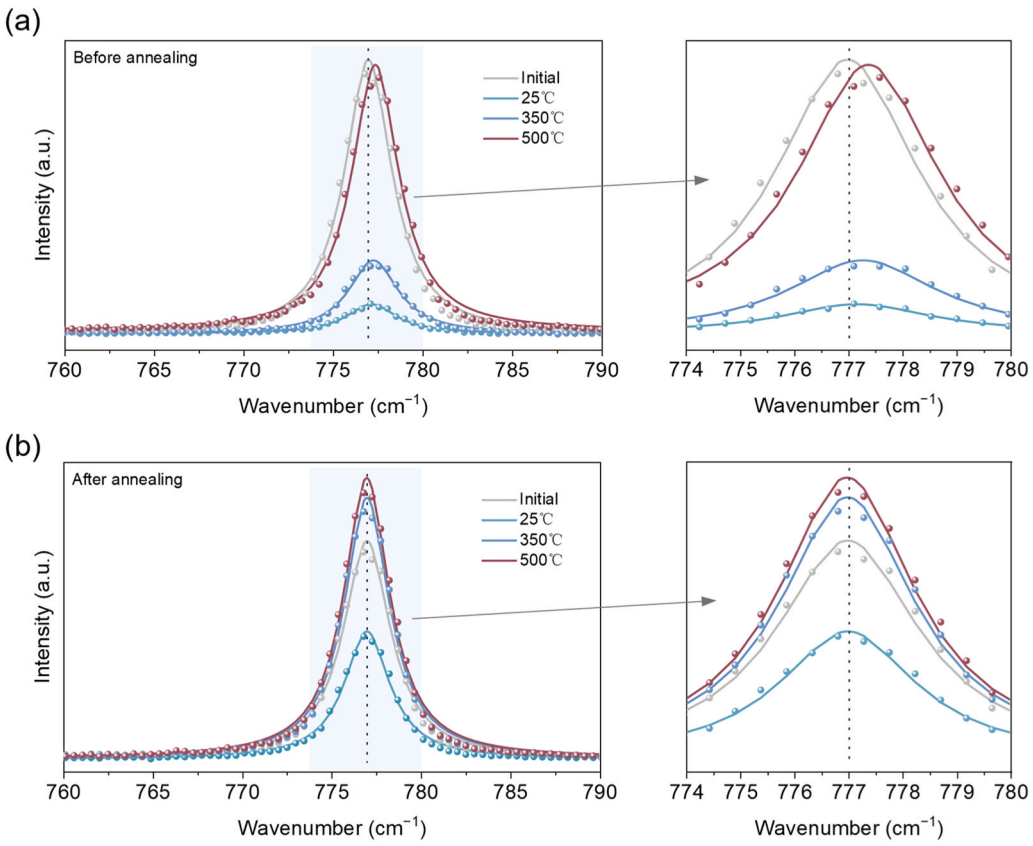


Fig. 16. E_2(TO) Raman peak of each sample (a) before annealing and (b) after annealing.

suppress lattice disorder and amorphization, they may simultaneously exacerbate residual compressive stress, potentially affecting stress-related reliability. Consequently, the optimal implantation temperature should be selected based on the dominant performance objective and reliability constraints. After high-temperature annealing, the E_2(TO) peak shifts were eliminated, reflecting substantial stress relief (Fig. 16b).

The specific direct relationship between Raman shift and residual stress is established through lattice dynamics theory. We first define the [1 −100], [11 −20], and [0001] crystal directions of the 4H-SiC crystal as X, Y, and Z axes, respectively. For 4H-SiC with a hexagonal crystal structure, the Raman tensor of its E_2(TO) mode exhibits double degeneracy. [63] Therefore, the lattice dynamics characteristic equation of 4H-SiC under a stress-strain field can be expressed as:

$$\begin{vmatrix} a_{E_2}(\varepsilon_{xx}+\varepsilon_{yy})+b_{E_2}\varepsilon_{zz}+c_{E_2}(\varepsilon_{xx}-\varepsilon_{yy})-\Delta\omega_{E_2} & 2c_{E_2}\varepsilon_{xy} \\ 2c_{E_2}\varepsilon_{xy} & a_{E_2}(\varepsilon_{xx}+\varepsilon_{yy})+b_{E_2}\varepsilon_{zz}-c_{E_2}(\varepsilon_{xx}-\varepsilon_{yy})-\Delta\omega_{E_2} \end{vmatrix} = 0 \tag{2}$$

where a_{E2}, b_{E2}, and c_{E2} are the phonon deformation potential constants of the E_2(TO) mode, ε_{uv} ($u, v = x, y$) are the strain components, and $\Delta\omega_{E2}$ is the E_2(TO) Raman peak shift. The relationship between Raman shift and stress for 4H-SiC is derived as:

$$\Delta\omega_{E_2} = a_{E_2}(\varepsilon_{xx}+\varepsilon_{yy})+b_{E_2}\varepsilon_{zz} \pm c_{E_2}\sqrt{(\varepsilon_{xx}-\varepsilon_{yy})^2+4\varepsilon_{xy}^2} \tag{3}$$

For a thin wafer primarily under in-plane (equibiaxial) stress, the shear stress can be ignored [64], simplifying the stress-strain conversion (Eq. (3)). Therefore, combined with the generalized Hooke's law, the stress-strain conversion equation of 4H-SiC under the in-plane stress state is obtained:

$$\begin{pmatrix} \varepsilon_{xx} \\ \varepsilon_{yy} \\ \varepsilon_{zz} \\ 2\varepsilon_{yz} \\ 2\varepsilon_{zx} \\ 2\varepsilon_{xy} \end{pmatrix} = \begin{pmatrix} s_{11} & s_{12} & s_{13} & & & \\ s_{12} & s_{11} & s_{13} & & & \\ s_{13} & s_{13} & s_{33} & & & \\ & & & s_{44} & & \\ & & & & s_{44} & \\ & & & & & s_{66} \end{pmatrix} \begin{pmatrix} \Delta\sigma_{xx} \\ \Delta\sigma_{yy} \\ 0 \\ 0 \\ 0 \\ 0 \end{pmatrix} = \begin{pmatrix} s_{11}\Delta\sigma_{xx}+s_{12}\Delta\sigma_{yy} \\ s_{12}\Delta\sigma_{xx}+s_{11}\Delta\sigma_{yy} \\ s_{13}(\Delta\sigma_{xx}+\Delta\sigma_{yy}) \\ 0 \\ 0 \\ 0 \end{pmatrix} \tag{4}$$

where s_{wx} ($w, x = 1, 2, 3, 4, 5, 6$) are the compliance coefficient components, and $\Delta\sigma_{uv}$ ($u, v = x, y$) are the stress components.

Then, the specific conversion relationship between Raman phonon displacement and stress was obtained [65]:

$$\begin{aligned} \Delta\omega_{E_2} &= 2[a_{E_2}(s_{11}+s_{12})+b_{E_2}s_{13}]\times\Delta\sigma \\ \Delta\sigma_{\text{in-plane}}(\text{MPa}) &= -323\times\Delta\omega_{\text{obs}}(\text{cm}^{-1}) \end{aligned} \tag{5}$$

where $\Delta\omega_{\text{obs}}$ is the peak displacement obtained from the Raman test.

To further evaluate the specific stress distribution state on the 6-inch 4H-SiC wafer, the Raman mapping was performed on each wafer. The distribution of E_2(TO) peak shift on the surface of each sample is shown

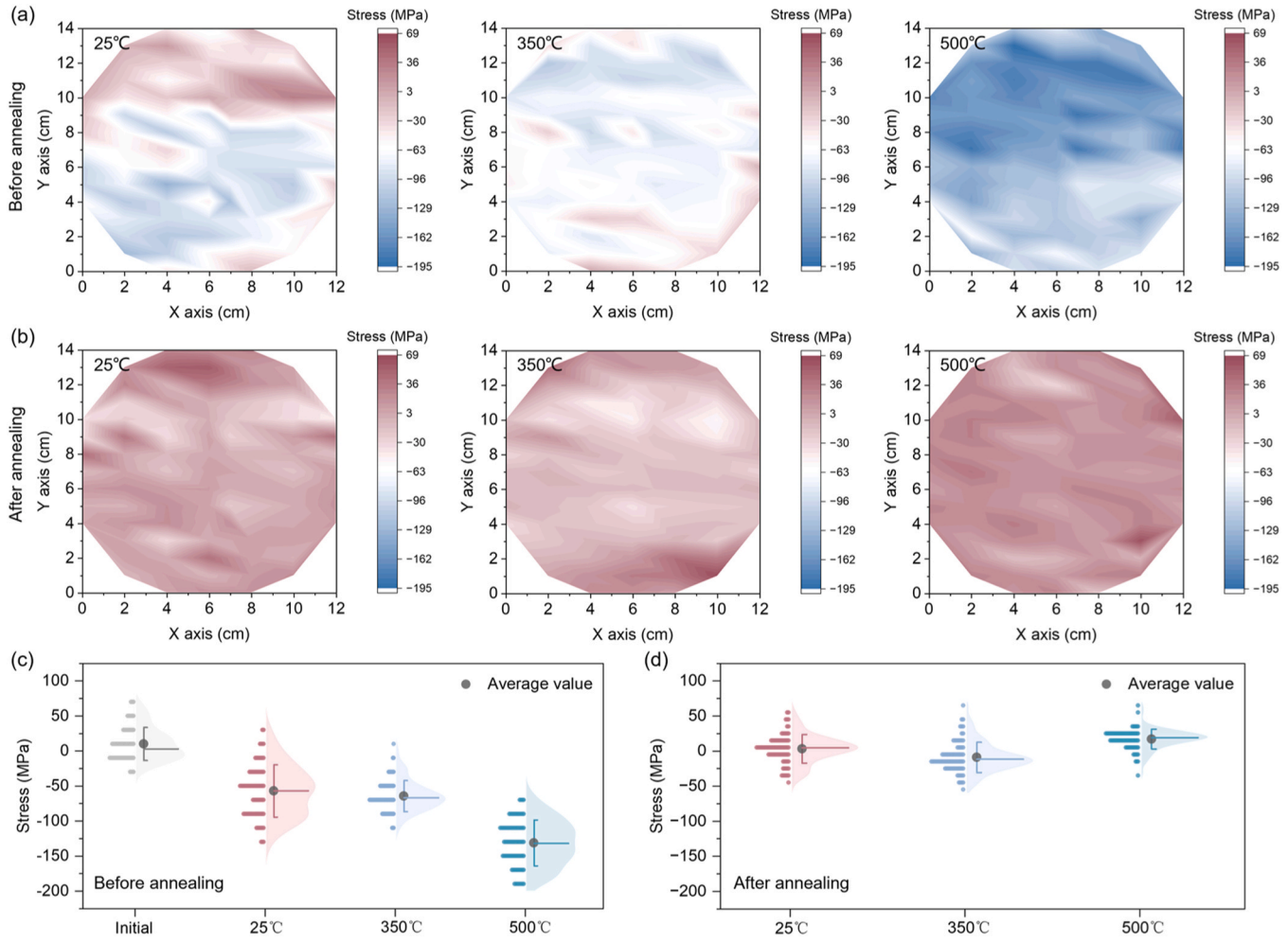


Fig. 17. Residual stress analysis at different Al ion implantation temperatures (a) after Al ion implantation and (b) after annealing. (c, d) Corresponding stress statistics for the implanted and annealed states.

in Fig. S7. Based on Eq. (5), converting these shifts to stress (Fig. 17a and c) revealed that the control wafer exhibited negligible stress (Fig. S8), whereas implanted wafers exhibited compressive stress that rose with increasing implantation temperature. This trend is consistent with the HRXRD observations reported by Chen et al. [66], where higher implantation temperatures reduce the out-of-plane tensile strain along the 4H-SiC c-axis, implying a corresponding increase in the in-plane compressive stress. Average residual stress values were −57 MPa, −64 MPa, and −132 MPa for implantation temperatures of 25°C, 350°C, and 500°C, respectively. This temperature-dependent increase in compressive residual stress is qualitatively consistent with the MD-predicted stress trend in Fig. 8b, i.e., higher implantation temperatures lead to stronger net compressive stress accumulation. Furthermore, the relatively similar average stresses for the 25°C and 350°C cases can be attributed to a more heterogeneous stress field (local compressive and tensile regions coexisting) that partially compensates in the spatial average, while the 500°C case exhibits a more uniformly compressive field and higher crystallinity in the implanted region, leading to a more negative averaged stress value. We attribute this temperature-dependent stress increase to defect recombination and temperature-assisted local structural rearrangement/lattice relaxation during implantation [67]. After high-temperature annealing, the residual stress was substantially released, ultimately approaching near zero as defects were repaired and the periodic crystal structure was restored (Fig. 17b and d).

Overall, both the lattice damage and residual stress analyses confirm that higher implantation temperatures reduce structural amorphization while increasing compressive stress, which can be alleviated by high-temperature annealing. These findings are trend-wise consistent with the MD results (Fig. 8b), underscoring the reliability of the predictive model and the importance of temperature control in optimizing the Al ion implantation process for 4H-SiC.

4. Conclusions

In summary, we present a nondestructive, multiscale approach that employs MD simulations and confocal micro-Raman measurements to elucidate how implantation temperature regulates defect, amorphization, and residual-stress evolution in CVD 4H-SiC. The MD results show that higher implantation temperatures suppress amorphization and promote Al–Si substitution, albeit at the expense of more compressive residual stress. Raman peak shifts, linewidths, and amorphization signatures provide quantitative, spatially resolved proxies for lattice disorder and phonon lifetime, tracking the coupled evolution of lattice disorder and stress. A key future direction is to systematically investigate more implantation temperatures and jointly optimize lattice-damage suppression and residual-stress control to identify processing windows that satisfy device-specific reliability constraints. Beyond the specific system studied, the combined simulation–optical metrology paradigm is readily applicable to other wide-bandgap compounds (e.g., GaN, AlN, β-Ga_2O_3), offering a materials-centric route to compare amorphization kinetics, defect recovery, and stress control across different systems.

Collectively, these insights define controllable thermal-treatment regimes that balance disorder suppression with stress management and offer a potential approach for nondestructive assessment of implantation-induced damage in compound semiconductors.

CRediT authorship contribution statement

Xinyue Wang: Writing – review & editing, Methodology, Formal analysis. **Yuanhui Zuo:** Writing – review & editing, Software, Resources, Project administration, Funding acquisition. **Zhoudong Yang:** Writing – original draft, Visualization, Investigation, Formal analysis, Data curation. **Botao Sun:** Validation, Resources, Methodology. **Jiajie Fan:** Writing – review & editing, Supervision, Project administration, Funding acquisition, Conceptualization. **Zhuorui Tang:** Resources. **Guoqi Zhang:** Resources. **Hongyu Tang:** Writing – review & editing. **Changran Zheng:** Software.

Declaration of Competing Interest

The authors declare that they have no known competing financial interests or personal relationships that could have appeared to influence the work reported in this paper.

Acknowledgments

This work was partially supported by the National Natural Science Foundation of China (Grant No. 52275559 and 62401157), China Scholarship Council (Grant No. 202406100064), and the Merit-based Zhejiang Province Postdoctoral Research Project (Grant No. ZJ2023118). Part of the experimental work was carried out at the Fudan Nanofabrication Laboratory.

Appendix A. Supporting information

Supplementary data associated with this article can be found in the online version at doi:10.1016/j.jallcom.2026.186279.

Data Availability

Data will be made available on reasonable request.

References

[1] E. Arduca, M. Perego, Doping of silicon nanocrystals, Mater. Sci. Semicond. Process 62 (2017) 156–170, https://doi.org/10.1016/j.mssp.2016.10.054.
[2] D.M. Lukin, M.A. Guidry, J. Vučković, Integrated quantum photonics with silicon carbide: challenges and prospects, PRX Quantum 1 (2) (2020) 020102, https://doi.org/10.1103/PRXQuantum.1.020102.
[3] A. Yi, C. Wang, L. Zhou, Y. Zhu, S. Zhang, T. You, J. Zhang, X. Ou, Silicon carbide for integrated photonics, Appl. Phys. Rev. 9 (3) (2022) 031302, https://doi.org/10.1063/5.0079649.
[4] R.B. Fair, J.J. Wortman, J. Liu, Modeling rapid thermal diffusion of arsenic and boron in silicon, J. Electrochem. Soc. 131 (10) (2019) 2387–2394, https://doi.org/10.1149/1.2115263.
[5] C.S. Nichols, C.G. Van de Walle, S.T. Pantelides, Mechanisms of dopant impurity diffusion in silicon, Phys. Rev. B Condens Matter 40 (8) (1989) 5484–5496, https://doi.org/10.1103/physrevb.40.5484.
[6] D. Yan, A. Cuevas, J. Stuckelberger, E.C. Wang, S.P. Phang, T.C. Kho, J.I. Michel, D. Macdonald, J. Bullock, Silicon solar cells with passivating contacts: classification and performance, Prog. Photo 31 (4) (2022) 310–326, https://doi.org/10.1002/pip.3574.
[7] X. She, A.Q. Huang, O. Lucia, B. Ozpineci, Review of silicon carbide power devices and their applications, IEEE Trans. Ind. Electron 64 (10) (2017) 8193–8205, https://doi.org/10.1109/tie.2017.2652401.
[8] Y. Zheng, M. Pu, A. Yi, B. Chang, T. You, K. Huang, A.N. Kamel, M.R. Henriksen, A. A. Jorgensen, X. Ou, H. Ou, High-quality factor, high-confinement microring resonators in 4H-silicon carbide-on-insulator, Opt. Express 27 (9) (2019) 13053–13060, https://doi.org/10.1364/OE.27.013053.
[9] K. Chen, S. Yang, J. Wang, G. Li, L. Sun, X. Xie, X. Yang, Y. Peng, X. Chen, X. Hu, X. Xu, Identification and formation mechanism of threading screw dislocations in 4H-SiC crystal, J. Alloy. Compd. 1040 (2025) 183454, https://doi.org/10.1016/j.jallcom.2025.183454.
[10] X. Wang, X. Xie, L. Zhao, G. Zhong, X. Chen, L. Sun, J. Tian, J. Wang, Y. Zhang, X. Yang, X. Hu, X. Xu, Induction frequency modulation for 4H-SiC growth: thermal field evolution, dislocation suppression, and high-quality crystal preparation via PVT method, J. Alloy. Compd. 1036 (2025) 181846, https://doi.org/10.1016/j.jallcom.2025.181846.
[11] Y. Zheng, M. Pu, A. Yi, X. Ou, H. Ou, 4H-SiC microring resonators for nonlinear integrated photonics, Opt. Lett. 44 (23) (2019) 5784–5787, https://doi.org/10.1364/OL.44.005784.
[12] Z. Cheng, J. Liang, K. Kawamura, H. Zhou, H. Asamura, H. Uratani, J. Tiwari, S. Graham, Y. Ohno, Y. Nagai, T. Feng, N. Shigekawa, D.G. Cahill, High thermal conductivity in wafer-scale cubic silicon carbide crystals, Nat. Commun. 13 (1) (2022) 7201, https://doi.org/10.1038/s41467-022-34943-w.
[13] X. Chen, X. Yang, X. Xie, Y. Peng, L. Xiao, C. Shao, H. Li, X. Hu, X. Xu, Research progress of large size SiC single crystal materials and devices, Light Sci. Appl. 12 (1) (2023) 28, https://doi.org/10.1038/s41377-022-01037-7.
[14] A. Hallén, M. Linnarsson, Ion implantation technology for silicon carbide, Surf. Coat. Technol. 306 (2016) 190–193, https://doi.org/10.1016/j.surfcoat.2016.05.075.
[15] F. Roccaforte, P. Fiorenza, M. Vivona, G. Greco, F. Giannazzo, Selective doping in silicon carbide power devices, Mater. (Basel) 14 (14) (2021) 3923, https://doi.org/10.3390/ma14143923.
[16] Y. Kang, Y. Pei, D. He, H. Xu, M. Ma, J. Yan, C. Jiang, W. Li, X. Xiao, Spatially selective p-type doping for constructing lateral WS_2 p-n homojunction via low-energy nitrogen ion implantation, Light Sci. Appl. 13 (1) (2024) 127, https://doi.org/10.1038/s41377-024-01477-3.
[17] W. Li, X. Zhan, X. Song, S. Si, R. Chen, J. Liu, Z. Wang, J. He, X. Xiao, A review of recent applications of ion beam techniques on nanomaterial surface modification: Design of nanostructures and energy harvesting, Small 15 (31) (2019) e1901820, https://doi.org/10.1002/smll.201901820.
[18] S. Takitani, A. Baba, H. Nishizawa, K. Suzuki, An efficient polishing process for silicon carbide using ion implantation method, Jpn. J. Appl. Phys. 63 (3) (2024) 038006, https://doi.org/10.35848/1347-4065/ad308c.
[19] J.F. Ziegler, M.D. Ziegler, J.P. Biersack, SRIM – The stopping and range of ions in matter (2010), Nucl. Instrum. Methods Phys. Res. B 268 (11-12) (2010) 1818–1823, https://doi.org/10.1016/j.nimb.2010.02.091.
[20] Z. Yang, X. Wang, Y. Zuo, Z. Tang, B. Guo, J. Zhang, H. Tang, R. Zhang, X. Fan, G. Zhang, J. Fan, Prediction of temperature-dependent stress in 4H-SiC using in situ nondestructive Raman spectroscopy characterization, Laser Photonics Rev. 19 (3) (2024) 2401033, https://doi.org/10.1002/lpor.202401033.
[21] J. Wong-Leung, M.S. Janson, A. Kuznetsov, B.G. Svensson, M.K. Linnarsson, A. Hallén, C. Jagadish, D.J.H. Cockayne, Ion implantation in 4H–SiC, Nucl. Instrum. Methods Phys. Res. B 266 (8) (2008) 1367–1372, https://doi.org/10.1016/j.nimb.2007.12.049.
[22] I. Choi, H.Y. Jeong, H. Shin, G. Kang, M. Byun, H. Kim, A.M. Chitu, J.S. Im, R. S. Ruoff, S.Y. Choi, K.J. Lee, Laser-induced phase separation of silicon carbide, Nat. Commun. 7 (2016) 13562, https://doi.org/10.1038/ncomms13562.
[23] Y. Zhai, H. Li, H. Wu, Z. Tao, G. Xu, X. Cao, T. Xu, Application of bulk silicon carbide technology in high temperature MEMS sensors, Mater. Sci. Semicond. Process 173 (2024) 108137, https://doi.org/10.1016/j.mssp.2024.108137.
[24] L. Kuebler, E. Hershkovitz, D. Kouzminov, H.J. Gossmann, S. Charnvanichborikarn, C. Hatem, H. Kim, K.S. Jones, 4H to 3C polytypic transformation in Al^+ implanted SiC during high temperature annealing, Electron. Mater. Lett. 20 (3) (2023) 345–351, https://doi.org/10.1007/s13391-023-00473-w.
[25] K. Ishiji, M. Arita, M. Adachi, R. Sugie, Y. Morita, T. Araki, Effect of carbon coating on surface structure in annealing process of high-dose implanted/annealed SiC, J. Appl. Phys. 135 (18) (2024) 185703, https://doi.org/10.1063/5.0205320.
[26] M. Usman, M. Nour, A.Y. Azarov, A. Hallén, Annealing of ion implanted 4H–SiC in the temperature range of 100–800°C analysed by ion beam techniques, Nucl. Instrum. Methods Phys. Res. B 268 (11-12) (2010) 2083–2085, https://doi.org/10.1016/j.nimb.2010.02.020.
[27] S. Kunj, K. Sreenivas, Residual stress and defect content in magnetron sputtered ZnO films grown on unheated glass substrates, Curr. Appl. Phys. 16 (7) (2016) 748–756, https://doi.org/10.1016/j.cap.2016.04.008.
[28] C. Chen, T. Zhang, Y. Lei, J. Fan, L. Zhang, G. Wang, L. Gao, P. Li, Q. Zhu, X. Ma, Y. Hao, Application and prospect of in situ TEM in wide bandgap semiconductor materials and devices, Appl. Phys. Rev. 12 (1) (2025) 011326, https://doi.org/10.1063/5.0225128.
[29] M. Belanche, Y. Yonezawa, R. Heller, A. Müller, C. Vockenhuber, C. Martinella, M. Rüb, M. Kato, K. Murata, H. Tsuchida, K. Nakayama, U. Grossner, Aluminum channeling in 4H-SiC by high-energy implantation above 10 MeV, Mater. Sci. Semicond. Process 179 (2024) 108461, https://doi.org/10.1016/j.mssp.2024.108461.
[30] M. Canino, P. Fedeli, C. Albonetti, R. Nipoti, 4H-SiC surface morphology after Al ion implantation and annealing with C-cap, J. Microsc. 280 (3) (2020) 229–240, https://doi.org/10.1111/jmi.12933.
[31] P. Kumar, M.I.M. Martins, M.E. Bathen, T. Prokscha, U. Grossner, Al-implantation induced damage in 4H-SiC, Mater. Sci. Semicond. Process 174 (2024) 108241, https://doi.org/10.1016/j.mssp.2024.108241.
[32] L. Sang, J. Xia, R. Jin, Y. Wang, Y. Zha, F. Yang, J. Wu, Ion implantation of aluminum in 4H-SiC epilayers from 90 keV to above 1 MeV, Solid State Electron 172 (2020) 107899, https://doi.org/10.1016/j.sse.2020.107899.
[33] J. Wong-Leung, M.S. Janson, B.G. Svensson, Effect of crystal orientation on the implant profile of 60 keV Al into 4H-SiC crystals, J. Appl. Phys. 93 (11) (2003) 8914–8917, https://doi.org/10.1063/1.1569972.
[34] Z. Yang, Y. Zuo, X. Wang, H. Zhou, H. Tang, C. Zheng, R. Zhang, Z. Tang, K. Dai, X. Fan, G. Zhang, J. Fan, Nondestructive analysis of interface damage and stress in

Al-ion implanted 4H-SiC homoepitaxial wafers via micro-Raman and multiscale simulation, Appl. Surf. Sci. 712 (2025) 164204, https://doi.org/10.1016/j.apsusc.2025.164204.
[35] F. Wu, J. Zhang, W. Xi, Y.-Q. Chi, Q.-B. Liu, L. Yang, H.-P. Ma, Q.-C. Zhang, Insights into the effects of Al-ion implantation temperature on material properties of 4H-SiC, Appl. Surf. Sci. 613 (2023) 156014, https://doi.org/10.1016/j.apsusc.2022.156014.
[36] J. Gao, T. Ju, L. Zhang, X. Kan, R. Ji, W. Tang, D. Fang, Z. Wei, X. Zhang, B. Zhang, Z. Zeng, Characterization of dislocation etch pits by molten KOH etching in n- and p-type 4H–SiC epilayers doped by ion implantation, Mater. Sci. Semicond. Process 165 (2023) 107647, https://doi.org/10.1016/j.mssp.2023.107647.
[37] F. Roccaforte, F. Giannazzo, G. Greco, Ion implantation doping in silicon carbide and gallium nitride electronic devices, Micro 2 (1) (2022) 23–53, https://doi.org/10.3390/micro2010002.
[38] Y. Fan, Z. Xu, Y. Song, B. Dong, Z. Xue, B. Liu, L. Liu, D. Tian, Nano material removal mechanism of 4H-SiC in ion implantation-assisted machining, Comput. Mater. Sci. 200 (2021) 110837, https://doi.org/10.1016/j.commatsci.2021.110837.
[39] Q. Kang, X. Fang, C. Wu, P. Verma, H. Sun, B. Tian, L. Zhao, S. Wang, N. Zhu, R. Maeda, Z. Jiang, Mechanical properties and indentation-induced phase transformation in 4H–SiC implanted by hydrogen ions, Ceram. Int. 48 (11) (2022) 15334–15347, https://doi.org/10.1016/j.ceramint.2022.02.067.
[40] Q. Kang, X. Fang, C. Wu, H. Sun, B. Tian, L. Zhao, S. Wang, Z. Jiang, N. Zhu, R. Maeda, M. Zhang, Y. Lv, Modification mechanism of collaborative ions implanted into 4H-SiC by atomic simulation and experiment, Int. J. Mech. Sci. 212 (2021) 106832, https://doi.org/10.1016/j.ijmecsci.2021.106832.
[41] X. Fang, X. Wu, Q. Kang, Z. Fang, H. Sun, C. Wu, Z. Zhang, P. Verma, R. Maeda, B. Tian, C. Kang, Atomistic analysis on implantation effects of hydrogen ions and copper ions into 4H-SiC, Appl. Surf. Sci. 665 (2024) 160329, https://doi.org/10.1016/j.apsusc.2024.160329.
[42] R. Devanathan, W.J. Weber, Displacement energy surface in 3C and 6H SiC, J. Nucl. Mater. 278 (2-3) (2000) 258–265, https://doi.org/10.1016/s0022-3115(99)00266-4.
[43] Y. Yang, C. Zhang, C. Su, Z. Ding, Y. Song, Damage and recovery behavior of 4H-SiC implanted with He ions, Nucl. Instrum. Methods Phys. Res. B 449 (2019) 54–57, https://doi.org/10.1016/j.nimb.2019.04.055.
[44] R.E. Stoller, M.B. Toloczko, G.S. Was, A.G. Certain, S. Dwaraknath, F.A. Garner, On the use of SRIM for computing radiation damage exposure, Nucl. Instrum. Methods Phys. Res. B 310 (2013) 75–80, https://doi.org/10.1016/j.nimb.2013.05.008.
[45] W. Wu, Y. Hu, X. Meng, J. Dai, H. Dai, Molecular dynamics simulation of ion-implanted single-crystal 3C-SiC nano-indentation, J. Manuf. Process 79 (2022) 356–368, https://doi.org/10.1016/j.jmapro.2022.04.071.
[46] S. Pal, M. Meraj, C. Deng, Effect of Zr addition on creep properties of ultra-fine grained nanocrystalline Ni studied by molecular dynamics simulations, Comput. Mater. Sci. 126 (2017) 382–392, https://doi.org/10.1016/j.commatsci.2016.10.013.
[47] S.Z. Chavoshi, X. Luo, Molecular dynamics simulation study of deformation mechanisms in 3C–SiC during nanometric cutting at elevated temperatures, Mater. Sci. Eng. A 654 (2016) 400–417, https://doi.org/10.1016/j.msea.2015.11.100.
[48] M. Ishimaru, I.T. Bae, Y. Hirotsu, S. Matsumura, K.E. Sickafus, Structural relaxation of amorphous silicon carbide, Phys. Rev. Lett. 89 (5) (2002) 055502, https://doi.org/10.1103/PhysRevLett.89.055502.
[49] Y. Wang, H. Lan, Q. Shangguan, Y. Lv, C. Jiang, A Multiscale Simulation on Aluminum Ion Implantation-Induced Defects in 4H-SiC MOSFETs, Electronics 13 (14) (2024) 2758, https://doi.org/10.3390/electronics13142758.
[50] T. Hornos, A. Gali, N.T. Son, E. Janzén, A theoretical study on aluminium-related defects in SiC, Mater. Sci. Forum 556-557 (2007) 445–448, https://doi.org/10.4028/www.scientific.net/MSF.556-557.445.
[51] C.M. Wang, Y. Zhang, W.J. Weber, W. Jiang, L.E. Thomas, Microstructural features of Al-implanted 4H–SiC, J. Mater. Res. 18 (4) (2012) 772–779, https://doi.org/10.1557/jmr.2003.0107.
[52] Z. Tao, Y. Song, L. Zhang, Z. Xu, Raman investigation of lattice anharmonicity and substrate-induced effects in AlN heteroepilayers, Ceram. Int. 49 (9) (2023) 14190–14201, https://doi.org/10.1016/j.ceramint.2023.01.007.
[53] X.L. Yang, X.F. Chen, Y. Peng, X.J. Xie, X.B. Hu, X.G. Xu, P. Yu, R.Q. Wang, Growth and temperature-depending Raman characterization of different nitrogen-doped 4H-SiC crystals, Mater. Sci. Forum 897 (2017) 307–310, https://doi.org/10.4028/www.scientific.net/MSF.897.307.
[54] X. Luo, X. Lu, C. Cong, T. Yu, Q. Xiong, S.Y. Quek, Stacking sequence determines Raman intensities of observed interlayer shear modes in 2D layered materials–A general bond polarizability model, Sci. Rep. 5 (2015) 14565, https://doi.org/10.1038/srep14565.
[55] K. Piskorski, M. Guziewicz, M. Wzorek, L. Dobrzański, Investigation of Al- and N-implanted 4H–SiC applying visible and deep UV Raman scattering spectroscopy, AIP Adv. 10 (5) (2020) 055315, https://doi.org/10.1063/1.5144579.
[56] Z.U. Rehman, K.A. Janulewicz, Structural transformations in femtosecond laser-processed n-type 4H-SiC, Appl. Surf. Sci. 385 (2016) 1–8, https://doi.org/10.1016/j.apsusc.2016.05.041.
[57] M.J. Madito, T.T. Hlatshwayo, C.B. Mtshali, Chemical disorder of a-SiC layer induced in 6H-SiC by Cs and I ions co-implantation: Raman spectroscopy analysis, Appl. Surf. Sci. 538 (2021) 148099, https://doi.org/10.1016/j.apsusc.2020.148099.
[58] S. Sorieul, J.M. Costantini, L. Gosmain, L. Thomé, J.J. Grob, Raman spectroscopy study of heavy-ion-irradiated α-SiC, J. Phys. Condens. Matter 18 (22) (2006) 5235–5251, https://doi.org/10.1088/0953-8984/18/22/022.
[59] R.N. Gontijo, N. Bunker, S.L. Graiser, X. Ding, M. Smeu, A.L. Elias, Resonant Raman scattering study of strain and defects in chemical vapor deposition grown MoS_2 monolayers, Small (2024) e2310685, https://doi.org/10.1002/smll.202310685.
[60] Z. Yang, X. Wang, W. Chen, H. Tang, R. Zhang, X. Fan, G. Zhang, J. Fan, Residual stress characterization in microelectronic manufacturing: an analysis based on Raman spectroscopy, Laser Photonics Rev. 18 (7) (2024) 2301300, https://doi.org/10.1002/lpor.202301300.
[61] H. Sakakima, S. Takamoto, Y. Murakami, A. Hatano, A. Goryu, K. Hirohata, S. Izumi, Development of a method to evaluate the stress distribution in 4H-SiC power devices, Jpn. J. Appl. Phys. 57 (10) (2018) 106602, https://doi.org/10.7567/jjap.57.106602.
[62] K. Shimada, K. Asada, M. Yodo, N. Ohtani, Raman scattering microscopy imaging of basal plane stacking faults and associated partial dislocations in 4H-SiC crystals, J. Appl. Phys. 127 (16) (2020) 165704, https://doi.org/10.1063/5.0007219.
[63] X. Qin, X. Li, X. Chen, X. Yang, F. Zhang, X. Xu, X. Hu, Y. Peng, P. Yu, Raman scattering study on phonon anisotropic properties of SiC, J. Alloy. Compd. 776 (2019) 1048–1055, https://doi.org/10.1016/j.jallcom.2018.10.324.
[64] B. Han, M. Sun, Y. Chang, S. He, Y. Zhao, C. Qu, W. Qiu, Raman characterization of the in-plane stress tensor of gallium nitride, Mater. (Basel) 16 (6) (2023) 2255, https://doi.org/10.3390/ma16062255.
[65] R. Sugie, T. Uchida, Determination of stress components in 4H-SiC power devices via Raman spectroscopy, J. Appl. Phys. 122 (19) (2017) 195703, https://doi.org/10.1063/1.5003613.
[66] Z.Y. Chen, H.Y. Peng, Y. Liu, Q.Y. Cheng, S. Hu, B. Raghothamachar, M. Dudley, R. Ghandi, S. Kennerly, P. Thieberger, Investigation of Lattice Strain in High Energy Implanted 4H-SiC Wafers by Al or N Atoms, Mater. Sci. Forum 1062 (2022) 361–365, https://doi.org/10.4028/p-m7sftq.
[67] N. Sellami, A. Debelle, M.W. Ullah, H.M. Christen, J.K. Keum, H. Bei, H. Xue, W. J. Weber, Y. Zhang, Effect of electronic energy dissipation on strain relaxation in irradiated concentrated solid solution alloys, Curr. Opin. Solid State Mater. Sci. 23 (2) (2019) 107–115, https://doi.org/10.1016/j.cossms.2019.02.002.